Thermodynamic, Kinetic, and Microstructure Data for Modeling Solidification of Fe-Al-Mn-Si-C Alloys

JYRKI MIETTINEN, SAMI KOSKENNISKA, VILLE-VALTTERI VISURI, MAHESH SOMANI, TIMO FABRITIUS, and JUKKA KÖMI

In this study, a set of thermodynamic, kinetic, and microstructure data is presented to simulate the non-equilibrium solidification of Fe-Al-Mn-Si-C alloys. The data were further validated with the experimental measurements and then used in a thermodynamic–kinetic software, IDS, to establish the effect of the alloying and cooling rate on the solidification behavior of high-AlMnSi (Al $\geq$ 0.5 wt pct, Mn $\geq$ 2 wt pct, Si $\geq$ 1 wt pct) steels. The modeling results were additionally validated by conducting electron probe microanalysis (EPMA) measurements. The results reveal that (1) solidification in high-AlMnSi steels occurs at much lower temperatures than in carbon steels; (2) increasing the cooling rate marginally lowers the solidus; (3) the microsegregation of Mn in austenite is much stronger than that of Si and Al due to the tendency of Al and Si to deplete from the liquid phase; (4) the residual delta ferrite content may be influenced by a proper heat treatment but not to the extent that could be expected solely from thermodynamic calculations; (5) in high-AlMnSi steels containing less than 0.2 wt pct carbon, the cracking tendency related to the strengthening above the solidus and the shell growth below the solidus may be much lower than in carbon steels.

I. INTRODUCTION

ADVANCED High-Strength Steels (AHSS) belonging to the family of Fe-Al-Mn-Si-C alloys have been extensively studied due to their high strength and good formability.[1] To control the continuous casting process, it is necessary to have a thermodynamic–kinetic software that can reproduce and interpolate measurement data with high accuracy. Modern solidification models apply computational thermodynamics and kinetic equations along with corresponding databases.[2] The reliability and self-consistency of the thermodynamic descriptions are especially important for the optimization routines. Furthermore, in online applications, the computational expense of the thermodynamic–kinetic description should be reasonably low, especially in 3D modeling applications.

The first aim of this investigation was to outline the necessary thermodynamic, kinetic, and microstructure data to conduct the thermodynamic–kinetic simulations for Fe-Al-Mn-Si-C alloys. To validate the modeling results, electron probe microanalysis (EPMA) measurements were taken. Finally, simulations were performed to investigate the solidification behavior of high-AlMnSi steels as a function of their compositions and cooling rate/s. Also simulated, below the solidus, were the ferrite/austenite transformations and the solute microsegregation, including the determination of the soluble grain boundary compositions. As these compositions, instead of the nominal ones, are expected to control the start of austenite decomposition,[3] they will play an important role in a later study, in which we plan to extend the current simulation work on high-AlMnSi (Al $\geq$ 0.5 wt pct, Mn $\geq$ 2 wt pct, Si $\geq$ 1 wt pct) steels to their austenite decomposition process. These simulations will apply new continuous cooling transformation (CCT) equations, which take into account the Al alloying that was not considered in the previously optimized CCT equations of Miettinen *et al.*[3]

A. *IDS Tool*

The developed descriptions are implemented in the IDS software,[4–7] which is a thermodynamic–kinetic software for the simulation of phase change, compound formation/dissolution, and solute distribution during the

JYRKI MIETTINEN, VILLE-VALTTERI VISURI, and TIMO FABRITIUS are with the Process Metallurgy Research Unit, University of Oulu, PO Box 4300, 90014 Oulu, Finland. Contact e-mail: ville-valtteri.visuri@oulu.fi SAMI KOSKENNISKA, MAHESH SOMANI, and JUKKA KÖMI are with the Materials and Mechanical Engineering Research Unit, University of Oulu, PO Box 4200, 90014 Oulu, Finland.

solidification of steels and their cooling/heating process after solidification. The package also simulates the solid-state phase transformations related to the austenite decomposition process below 900 °C (1173 K) and calculates important thermophysical material properties (such as enthalpy, thermal conductivity, and density) from the liquid state to room temperature. The calculations of the IDS tool have been compared with numerous solidification-related measurements that show generally good agreement. Coupled with a suitable heat transfer model,[8] the IDS software is applicable for the online simulation of the continuous casting process.

Assuming complete solute mixing in the liquid and a regular dendritic structure, the calculations can be made in one volume element set on the side of a dendrite arm (Figure 1). At the same time, of course, no solute exchange is allowed between the volume element and its surroundings. Using a hexagonal arm arrangement for the dendrites,[9] the volume element assumes the form of an equilateral triangle when looking perpendicularly to the dendrite arm growth. All calculations are made stepwise,[6] decreasing the temperature in the liquid region in steps of 1 °C, decreasing the liquid fraction in the mushy zone by the 67 steps into which the volume element is divided, and decreasing or increasing the temperature in the solid state (below the solids) in steps of 1 °C, depending on whether the steel is cooled or heated. Other assumptions simplifying the calculations are (1) the thermodynamic equilibrium holds good at the solution phase interfaces; (2) the diffusion of solutes is independent of the chemical effect of other solutes; (3) differences in the molar volumes of the phases are negligible; (4) during solidification, both ferrite and austenite begin to form as soon as it is thermodynamically possible.
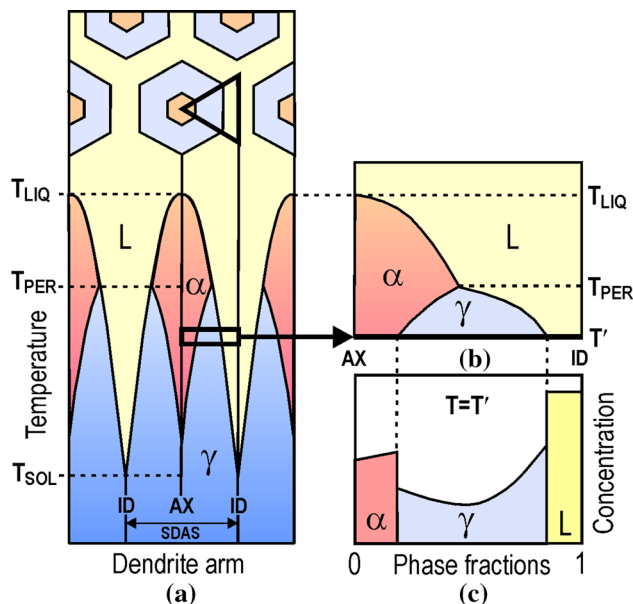

Fig. 1—Volume element on the side of a secondary dendrite arm (a) and some results of simulation: (b) phase fractions; (c) solute concentration profiles. L liquid, α ferrite, γ austenite, T_{LIQ} liquidus temperature, T_{PER} peritectic temperature, T_{SOL} solidus temperature, AX dendrite arm axis, ID interdendritic region, SDAS secondary dendrite arm spacing.

Depending on the composition, the solidifying Fe-Al-Mn-Si-C alloys go through one of the following solidification paths down to 900 °C (1173 K) prior to the austenite decomposition:

(A) L → L + α → α → γ + α(→ γ),
(B) L → L + α → L + γ + α → γ + α (→ γ),
(C) L → L + γ → γ,

where L denotes liquid, α denotes ferrite, and γ denotes austenite. The mutual order of the phases in the above paths shows how the phases are located in the volume element of Figure 1, from the dendrite arm axis (left) to the interdendritic region (right). In the two-phase regions of L + α, L + γ, and γ + α, subsequent transformations of L → α, L→γ, and α → γ, respectively, occur during cooling, and in the three-phase region of L + γ + α, a peritectic transformation of L + α → γ occurs. Note that the solid structure at 900 °C (1173 K) may contain the austenite and ferrite, and not necessarily only the austenite (see paths A and B).

Three thermodynamic models are employed in the calculations: (1) the substitutional solution model for the solution phases,[10] i.e., liquid (L), ferrite (α), and austenite (γ); (2) the magnetic ordering model of Hillert and Jarl[11] for ferrite; and (3) the sublattice model[10] for the semi-stoichiometric compounds. Strictly speaking, the chemical potentials that are specific functions based on the models rather than the models themselves are applied in the calculations to determine the thermodynamic equilibrium at the phase interfaces. The kinetics is taken into account by the solute material balance equations and Fick's diffusion laws. The corresponding expressions include the solute diffusion coefficients and the dendrite arm spacing, representing the diffusion distance in the microstructure. Also included, of course, is the time (diffusion time), which is derived from the cooling/heating process. For a detailed description of the calculation strategy and the corresponding equations, the reader is guided to the authors' previous papers.[5,6] The thermodynamic, kinetic, and microstructure data required in these calculations are stored in the extensive databank of the model. The current databank contains data for the elements Fe, C, Si, Mn, P, S, Cr, Mo, Ni, Cu, Al, N, Nb, Ti, V, Ca, Ce, Mg, B, O, and H.

In the following, calculation equations are introduced to demonstrate the IDS simulation of purely austenitic solidification, without the formation of inclusions. In this case, we use the following set of equations:

$$\mu_i^{\gamma}(T, x_1^{\gamma}, \ldots, x_n^{\gamma}) = \mu_i^{L}(T, x_1^{L}, \ldots, x_n^{L}) \quad (i = 1, \ldots, n) \tag{1}$$

$$\Delta f^{L}(x_i^{L0} - x_i^{\gamma}) = f^{L}(x_i^{L} - x_i^{L0}) - S_i^{\gamma/L}(T, x_i^{\gamma}, D_i^{\gamma}) \\ (i = 2, \ldots, n), \tag{2}$$

where μ_i^{ϕ} is the chemical potential of the component i in phase ϕ, x_i^{ϕ} is the interface composition of component i in phase ϕ (in mole fraction), T is the temperature (in K), n is the number of components in the alloy (with $i = 1$ for Fe), f^{L} is the liquid fraction, Δf^{L}

is the fractional movement of the γ/L interface, and x_i^{L0} is the liquid composition before movement Δf^L. The term $S_i^{\phi1/\phi2}$ includes Fick's first law of diffusion and describes the amount of material in the γ phase leaving the γ/L interface. Its general form in this presentation is $S_i^{\gamma/L} = -4 \cdot D_i^{\gamma} \cdot \Delta t \cdot G_i^{\gamma/L} \cdot SDAS^{-2}$, where D_i^{γ} is the diffusion coefficient of solute i in the γ phase, Δt is the time spent during the fractional movement of the γ/L interface, $G_i^{\gamma/L}$ is the dimensionless concentration gradient at the γ/L interface, and SDAS is the secondary dendrite arm spacing. The time increment Δt is related to temperature T as $\Delta t = (T^0 - T)/CRT$, where T^0 is the temperature of the previous calculation step, and CRT is the cooling rate of the process. Similar sets of equations also hold for the α/L and the α/γ interfaces. After solving Eqs. [1] and [2] at a certain step (*i.e.*, at a certain liquid fraction value), we simulate the change of solute concentrations in austenite between the α/L and the α/γ interfaces. This is done by applying an implicit finite difference method to the solution of Fick's 2nd law

$$\frac{\partial x_i^{\varphi}}{\partial t} = D_i^{\varphi} \frac{\partial^2 x_i^{\varphi}}{\partial z^2} \quad (i = 2, \ldots, n), \quad [3]$$

using the previously obtained time increment of Δt and distance $\Delta z = SDAS/2$ in its solution. As a result, we obtain the dimensionless concentration gradient at the γ/L interface, $G_i^{\gamma/L}$, required to solve Eqs. [1] and [2] at the next liquid fraction value.

Note that applying simplification (2) makes the solution of Fick's diffusion laws very simple. Truly, in ternary and higher-order systems, one should solve the diffusion problem with generalized Fick's laws containing both diagonal and off-diagonal diffusion coefficients, D_{ii} and D_{ij}, whereas the above equations apply only the diagonal coefficients. The numerical treatment of multicomponent diffusion has been successfully developed by Ågren and co-workers.[12–17] Their method improves the accuracy of simulation, particularly in the processes of long duration (*e.g.*, diffusion couple experiments and dissolution of phases at low temperatures). In solidification, however, the total available time for diffusion is usually short. In such a process, one can simplify the calculations by ignoring the effect of the off-diagonal diffusion coefficients, as their values are usually considerably smaller than those of the diagonal terms.

II. MODELING DATA

A. *Thermodynamic Data*

The thermodynamic data for the modeling of the solidification of Fe-Al-Mn-Si-C alloys are taken from a recent thermodynamic assessment of the Fe-Al-Mn-Si-C system[18] adopted in the Iron Alloy Database (IAD) developed since 2000. The main phases of that system and their modeling are shown in Table I.

In the present investigation, however, we show the thermodynamic data only for the three solution phases, liquid, ferrite, and austenite (Table II), because the other phases mentioned in Table I are hardly stable in

Table I. Phases and Their Thermodynamic Modeling in the Fe-Al-Mn-Si-C Description of Miettinen et al.[18]

Phase	Modeling
Liquid ($\approx$ L)	(Al,C,Fe,Mn,Si), substitutional, RK
Ferrite (α) with MOT	(Al,C,Fe,Mn,Si), substitutional, RK
Austenite (γ)	(Al,C,Fe,Mn,Si), substitutional, RK
M_3C ($\approx$ cementite)	(Fe,Mn)$_3$(C), sublattice, RK
M_5C_2	(Fe,Mn)$_5$(C)$_2$, sublattice, RK
M_7C_3	(Fe,Mn)$_7$(C)$_3$, sublattice, RK
Kappa ($\approx \kappa$)	(Al,Fe,Mn)$_7$(C), sublattice, RK
Graphite ($\approx$ gra)	pure C

RK denotes the Redlich–Kister treatment[19] for the Gibbs excess energy of the phase, and MOT denotes an additional magnetic ordering treatment for the α phase.[11]

typical Fe-Al-Mn-Si-C alloys above 900 °C (1173.15 K). The solution phase data, as listed in Table II, are applied in the present investigation to calculate the chemical potentials of the components as demonstrated in Reference 12.

Concerning the data in Table II, two essential assumptions have been made to simplify the simulations in the IDS tool. First, carbon in ferrite and austenite (strictly speaking, in the bcc and fcc structures, respectively) is treated as a substitutional component. In reality, carbon atoms occupy their own sublattice positions in these two-phase structures, which should therefore be modeled by a two-sublattice model.[10] This also concerns the magnetic ordering part of ferrite. However, applying the substitutional solution model to any component of the alloy makes the IDS simulation faster, without greatly reducing the reliability of the results (as indicated later in the text). A more detailed discussion of the advantages of this approach in online applications is available elsewhere.[18] The second simplification ignores the B2-ordering of ferrite (bcc structure) in alloys where the Al and Si contents are high. This treatment clearly simplifies the calculations of the IDS tool and is not a problem for typical steels, whose Al and Si contents are relatively low. Nevertheless, the energetic contribution due to the ordering effect has been added to the disordered part of the ferrite. This treatment enables the calculated ferrite containing phase equilibria of any Al and Si composition to fit the measurements given in the literature.

The solution phase thermodynamic data of Table II and the thermodynamic compound data of description[18] have been validated with an extensive amount of experimental data on phase equilibria, solute activity, and mixing enthalpy.[18] Some are presented in Figures 2 through 7, displaying good agreement between the calculations and measurements.[31–40]

Figures 2 and 7 show that increasing the Al and Si alloying contents clearly increases the ferrite stability in Fe-C alloys. This evidently affects both the high-temperature properties of the alloy and its austenite decomposition process at lower temperatures. The effect

Table II. Thermodynamic Description of the Liquid, Ferrite (α), and Austenite (γ) Phases of the Fe-Al-Mn-Si-C System[18]

Phase	References
Liquid (1 sublattice, sites: 1, constituents: Al, C, Fe, Mn, Si)	

$L^{L}_{Al,C} = (+\ 91{,}291 - 45.241T) + (+\ 50{,}958 - 45.241T)(x_{Al} - x_{C})$ — 21

$L^{L}_{Al,Fe} = (-\ 80{,}800 + 15T) + (-\ 5000 + 3T)(x_{Al} - x_{Fe}) + (+\ 4500 - 4T)(x_{Al} - x_{Fe})^{2}$ — 18

$L^{L}_{Al,Mn} = (-\ 66{,}174 + 27.099T) + (-\ 7509 + 5.484T)(x_{Al} - x_{Mn}) + (-\ 2639)(x_{Al} - x_{Mn})^{2}$ — 22

$L^{L}_{Al,Si} = (-\ 11{,}340 - 1.234T) + (-\ 3531 + 1.36T)(x_{Al} - x_{Si}) + (2265)(x_{Al} - x_{Si})^{2}$ — 23

$L^{L}_{C,Fe} = (-\ 124{,}320 + 28.5T) + (+\ 19{,}300)(x_{C} - x_{Fe}) + (+\ 49{,}260 - 19T)(x_{C} - x_{Fe})^{2}$ — 24

$L^{L}_{C,Mn} = (-\ 179{,}183 + 43.845T) + (+\ 6313)(x_{C} - x_{Mn}) + (+\ 23{,}281)(x_{C} - x_{Mn})^{2}$ — 25

$L^{L}_{C,Si} = (+\ 13{,}000 - 3T)$ — 18

$L^{L}_{Fe,Mn} = (-\ 3950 + 0.489T) + (+\ 1145)(x_{Fe} - x_{Mn})$ — 26

$L^{L}_{Fe,Si} = (-\ 164{,}435 + 41.977T) + (-\ 21.523T)(x_{Fe} - x_{Si}) + (5220 + 5.726T)(x_{Fe} - x_{Si})^{2} + (-\ 28{,}955 + 26.275T)(x_{Fe} - x_{Si})^{3}$ — 27

$L^{L}_{Mn,Si} = (-\ 139{,}817 + 29.861T) + (-\ 34{,}917 + 3.205T)(x_{Mn} - x_{Si}) + (+\ 46{,}782 - 18.19T)(x_{Mn} - x_{Si})^{2} + (+\ 16{,}168)(x_{Mn} - x_{Si})^{3}$ — 28

$L^{L}_{Al,C,Fe} = (+\ 20{,}000)x_{Al} + (-\ 60{,}000)x_{C} + (-\ 388{,}000 + 150T)x_{Fe}$ — 18

$L^{L}_{Al,Fe,Mn} = (-\ 20{,}000)x_{Al} + (+\ 0)x_{Fe} + (+\ 20{,}000)x_{Mn}$ — 18

$L^{L}_{Al,Fe,Si} = (-\ 30{,}000 - 30T)x_{Al} + (-\ 280{,}000 + 100T)x_{Fe} + (+\ 80{,}000)x_{Si}$ — 18

$L^{L}_{C,Fe,Mn} = (-\ 90{,}000)x_{C} + (+\ 50{,}000 - 20T)x_{Fe} + (+\ 30{,}000)x_{Mn}$ — 18

$L^{L}_{C,Fe,Si} = (+\ 200{,}000 + 90T)x_{C} + (-\ 300{,}000 + 90T)x_{Fe} + (+\ 60{,}000 + 90T)x_{Si}$ — 18

$L^{L}_{C,Mn,Si} = (+\ 200{,}000)x_{C} + (-\ 100{,}000)x_{Mn} + (+\ 100{,}000)x_{Si}$ — 18

$L^{L}_{Fe,Mn,Si} = (-\ 180{,}000 + 20T)x_{Fe} + (-\ 120{,}000 + 20T)x_{Mn} + (+\ 140{,}000 - 20T)x_{Si}$ — 18

$L^{L}_{Al,C,Fe,Mn} = (+\ 700{,}000 - 300T)$ — 18

$L^{L}_{Al,Fe,Mn,Si} = (+\ 200{,}000)$ — 18

$L^{L}_{C,Fe,Mn,Si} = (-\ 500{,}000)$ — 18

Ferrite (α) (1 sublattice, sites: 1, constituents: Al, C, Fe, Mn, Si)

$^{\circ}G^{\alpha}_{C} = {}^{\circ}G^{gra}_{C} + (+\ 107{,}350 + 35.764T)$ — 18

$L^{\alpha}_{Al,C} = 0$ — 18

$L^{\alpha}_{Al,Fe} = (-\ 128{,}300 + 35T) + (-\ 13{,}600 + 10T)(x_{Al} - x_{Fe})$ — 18

$L^{\alpha}_{Al,Mn} = (-\ 122{,}925 + 54.488T) + (-\ 78{,}760 + 53.245T)(x_{Al} - x_{Mn})$ — 29

$L^{\alpha}_{Al,Si} = L^{\gamma}_{Al,Si}$ — 18

$L^{\alpha}_{C,Fe} = (-\ 119.04T) + (-\ 43.886T)(x_{C} - x_{Fe}) + (-\ 7.858T)(x_{C} - x_{Fe})^{2}$ — 18

$L^{\alpha}_{C,Mn} = (-\ 155{,}000)$ — 18

$L^{\alpha}_{C,Si} = 0$ — 18

$L^{\alpha}_{Fe,Mn} = (-\ 2759 + 1.237T)$ — 25

$L^{\alpha}_{Fe,Si} = (-\ 211{,}000 + 80.2T) + (37{,}000 - 74.5T)(x_{Fe} - x_{Si}) + (-\ 10{,}000 + 41.2T)(x_{Fe} - x_{Si})^{2}$ — 18

$L^{\alpha}_{Mn,Si} = (-\ 89{,}621 + 2.941T) + (-\ 7500)(x_{Mn} - x_{Si})$ — 28

$L^{\alpha}_{Al,C,Fe} = (-\ 80{,}000 + 50T)$ — 18

$L^{\alpha}_{Al,Fe,Mn} = (+\ 26{,}000 - 10T)x_{Al} + (+\ 16{,}000 - 10T)x_{Fe} + (+\ 13{,}000)x_{Mn}$ — 18

$L^{\alpha}_{Al,Fe,Si} = (-\ 95{,}000)x_{Al} + (-\ 125{,}000)x_{Fe} + (-\ 95{,}000)x_{Si}$ — 18

$L^{\alpha}_{C,Fe,Mn} = (-\ 50{,}000)$ — 18

$L^{\alpha}_{C,Fe,Si} = (+\ 400{,}000)x_{C} + (-\ 25{,}000 - 100T)x_{Fe} + (+\ 400{,}000)x_{Si}$ — 18

$L^{\alpha}_{Fe,Mn,Si} = (-\ 100{,}000 - 30T)x_{Fe} + (+\ 10{,}000)x_{Mn} + (+\ 20{,}000)x_{Si}$ — 18

$L^{\alpha}_{Al,C,Fe,Mn} = (-\ 920{,}000 + 300T)$ — 18

$Tc^{\alpha} = 1043(x_{Fe} + x_{C}) - 580x_{Mn} + x_{Al}x_{Fe}(-\ 1100(x_{Al} - x_{Fe})) + x_{Fe}x_{Mn}(123) + x_{Fe}x_{Si}(504(x_{Fe} - x_{Si})) - 200x_{Fe}x_{C}$ — 18

$\beta^{\alpha} = 2.22(x_{Fe} + x_{C}) - 0.27x_{Mn}$ — 18

Austenite (γ) (1 sublattice, sites: 1, constituents: Al, C, Fe, Mn, Si)

$^{\circ}G^{\gamma}_{C} = {}^{\circ}G^{gra}_{C} + (+\ 155{,}005 + 13.703T)$ — 18

$L^{\gamma}_{Al,C} = 0$ — 18

$L^{\gamma}_{Al,Fe} = (-\ 84{,}100 + 17T) + (+\ 22{,}000)(x_{Al} - x_{Fe}) + (+\ 10{,}000)(x_{Al} - x_{Fe})^{2}$ — 18

$L^{\gamma}_{Al,Mn} = (-\ 79{,}521 + 34.8T) + (+\ 13{,}500 - 4.1T)(x_{Al} - x_{Mn})$ — 29

$L^{\gamma}_{Al,Si} = (-\ 3144 + 0.393T)$ — 23

$L^{\gamma}_{C,Fe} = (-\ 162{,}313 - 43.515T) + (-\ 60{,}802 - 17.241T)(x_{C} - x_{Fe}) + (-\ 10{,}956 - 3.306T)(x_{C} - x_{Fe})^{2}$ — 18

$L^{\gamma}_{C,Mn} = (-\ 245{,}200 + 3.5T) + (+\ 45{,}000)(x_{C} - x_{Mn})^{2}$ — 18

$L^{\gamma}_{C,Si} = 0$ — 18

$L^{\gamma}_{Fe,Mn} = (-\ 7762 + 3.865T) + (-\ 259)(x_{Fe} - x_{Mn})$ — 26

$L^{\gamma}_{Fe,Si} = (-\ 125{,}248 + 41.166T) + (-\ 142{,}708)(x_{Fe} - x_{Si}) + (+\ 89{,}907)(x_{Fe} - x_{Si})^{2}$ — 30

$L^{\gamma}_{Mn,Si} = (-\ 95{,}600 + 2.941T) + (-\ 7500)(x_{Mn} - x_{Si})$ — 28

$L^{\gamma}_{Al,C,Fe} = (-\ 345{,}000 + 100T)$ — 18

$L^{\gamma}_{Al,Fe,Mn} = (-\ 90{,}000 + 15T)x_{Al} + (-\ 25{,}000 + 15T)x_{Fe} + (-\ 15{,}000)x_{Mn}$ — 18

$L^{\gamma}_{Al,Fe,Si} = (-\ 50{,}000)$ — 18

$L^{\gamma}_{C,Fe,Mn} = (+\ 100{,}000)x_{C} + (+\ 100{,}000)x_{Fe} + (+\ 150{,}000)x_{Mn}$ — 18

$L^{\gamma}_{C,Fe,Si} = (-\ 320{,}000 + 100T)x_{C} + (-\ 233{,}000 + 100T)x_{Fe} + (-\ 500{,}000 + 100T)x_{Si}$ — 18

$L^{\gamma}_{Fe,Mn,Si} = (-\ 80{,}000 - 40T)$ — 18

Table II. continued

Phase	References
$L^{\gamma}_{Al,C,Fe,Mn} = (-920,000 + 300T)$	18
$L^{\gamma}_{Al,Fe,Mn,Si} = (-120,000)$	18

Gibbs energy data of pure components are given by Dinsdale[20] unless not shown in the Table. Parameter values except for T_c and β are in J/mol.
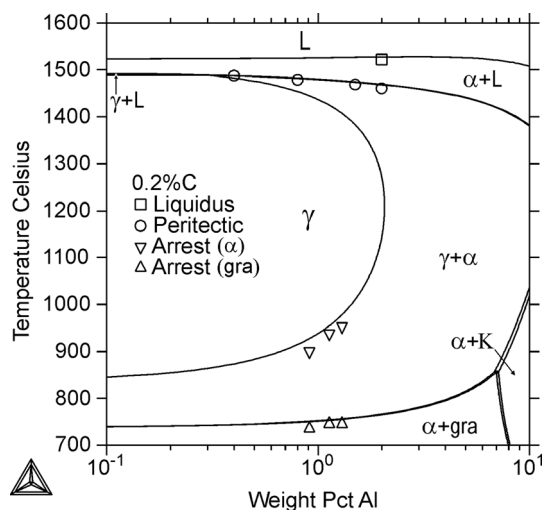

Fig. 2—Calculated[18] vertical section of 0.2 wt pct C in the Fe-Al-C system, with the experimental datapoints of Li et al.[31] for arrests and Presoly et al.[32] for peritectic and solidus.
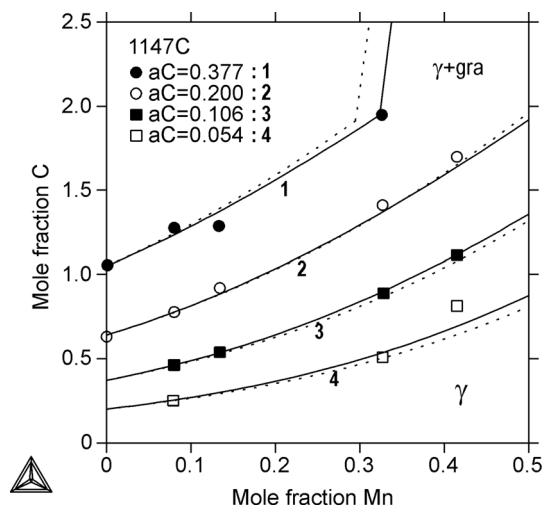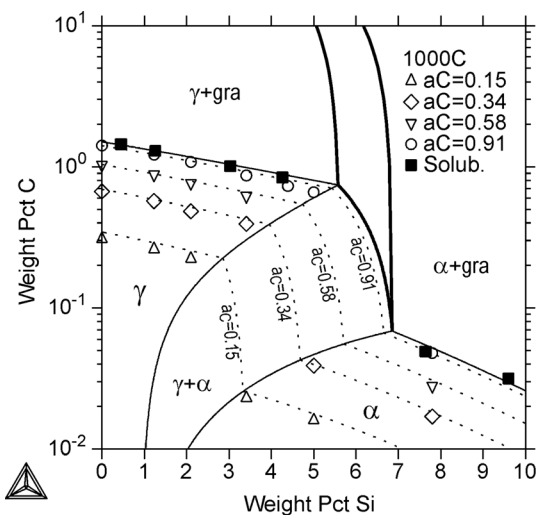

Fig. 4—Calculated[18] isotherm and carbon isoactivities (dotted lines) of the Fe-Si-C system at 1000 °C (1273 K), with the experimental datapoints of Smith[35] for carbon isoactivities, and Schürmann et al.[36] for graphite solubility.

Fig. 3—Calculated carbon isoactivities in γ Fe-Mn-C alloys at 1147 °C (1420 K), with the experimental datapoints of Wada et al.[33] Solid lines refer to the calculations of Miettinen et al.[18], and broken lines refer to those of Djurovic et al.[34] The reference state used is pure graphite C.

Figures 3 and 4 show that Mn alloying decreases and Si alloying increases the activity of carbon in austenite. This supports the widely accepted claim that C-Mn atom interactions are attractive, and C-Si atom interactions are repulsive. As the IDS can handle all such solute interactions while using a thermodynamic model, its simulations can be expected to progress in a controlled way. Even the previously stated simplification of the substitutional carbon atom poses no restriction here, because the results have been shown to be in excellent agreement with some earlier descriptions treating carbon as an interstitial solute.[18] This is proved especially by the calculated activities of carbon in ferrite and austenite. For example, Figure 3 shows negligible differences in the curves derived by Reference 18 and Djurovic et al.[34] The latter applied the two-sublattice model for ferrite and austenite.

Figure 5 shows the phase equilibria of the Fe-Al-Mn-C system at 1100 °C (1173 K) and 20 wt pct Mn. Also shown are the γ regions corresponding to 10 and 0 wt pct Mn, which reveal that Mn alloying increases the austenite stability. However, the γ region extends less toward the M₃C and Kappa phases, because Mn also stabilizes those phases. Also noteworthy is the line-compound-type appearance of the Kappa phase, which is due to its simple formulation of $(Al,Fe,Mn)_7(C)$ adopted in Reference 18. Indeed, its composition region (in Figure 5) is more circular, as assessed by Chin
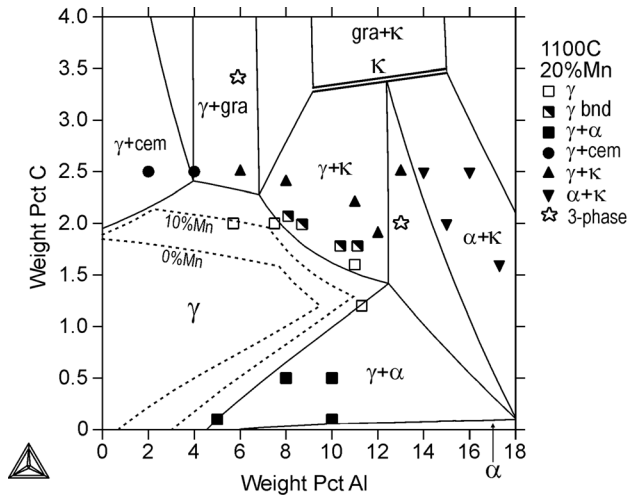
of cooling and heating on the ferrite stability in high-Al,Mn,Si steels is studied more closely in Section IV.

Fig. 5—Calculated[18] isotherm of the Fe-Al-Mn-C system at 1100 °C and 20 wt pct Mn, with the experimental datapoints of Ishida et al.[37] and Fartushna et al.[38] Bnd denotes a phase boundary. Broken lines show the calculated austenite region at 10 wt pct Mn and 0 wt pct Mn.
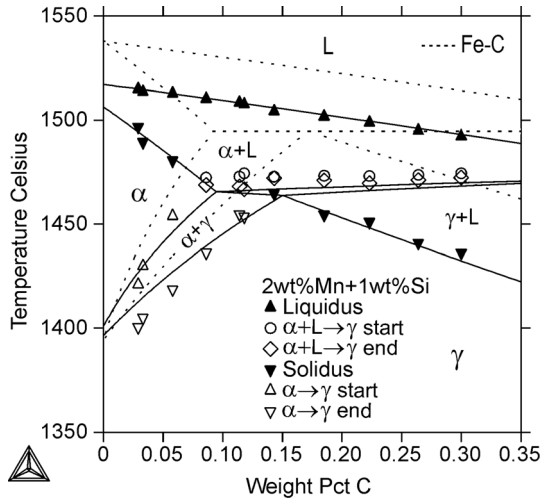

Fig. 6—Calculated[18] vertical section of 2 wt pct Mn and 1 wt pct Si in the Fe-Mn-Si-C system, with experimental datapoints of Presoly et al.[39] Broken lines show the calculated Fe-C phase diagram.

et al.[41] and Kim and Kang.[42] Nevertheless, as shown in Reference 18, the simple Kappa phase description works well in calculating the solubility of the Kappa phase in austenite. However, neither the M_3C nor the Kappa phase is involved in the phase equilibria of the steels considered in this study.

Figure 6 shows the vertical section of 2 wt pct Mn and 1 wt pct Si in the Fe-Mn-Si-C system. Also shown is the calculated Fe-C phase diagram, indicating how markedly the Mn and Si alloying of only 2 wt pct and 1 wt pct can drop the phase region positions to lower temperatures. Of course, during real solidification, this drop is even more dramatic because of the sluggish kinetics that delays the solidification process. An example calculation of this effect is presented in Section V.

B. Kinetic Data

The kinetic data for the modeling of solidification of Fe-Al-Mn-Si-C alloys consist of the binary diffusion coefficients of its solutes (Al, Mn, Si, C) in ferrite (α) and austenite (γ) structures. Using the experimental measurements shown in Table III, the following Arrhenius-type expressions were derived for the binary diffusion coefficients:

$$D^{\alpha}_{Al} = 5.03572 \exp\left[\frac{-(240,920 - 216,524 x^{\alpha}_{Al})}{RT}\right] \quad [4]$$

$$D^{\gamma}_{Al} = 0.18119 \cdot \exp\left[\frac{-253,560}{RT}\right] \quad [5]$$

$$D^{\alpha}_{C} = 0.11448 \cdot \exp\left[\frac{-95,612}{RT}\right] \quad [6]$$

$$D^{\gamma}_{C} = 0.22748 \cdot \exp\left[\frac{-(147,901 - 232,634 x^{\gamma}_{C})}{RT}\right] \quad [7]$$

$$D^{\alpha}_{Mn} = 0.64688 \cdot \exp\left[\frac{-222,320}{RT}\right] \quad [8]$$

$$D^{\gamma}_{Mn} = 0.15394 \cdot \exp\left[\frac{-(264,583 - 42,912 x^{\gamma}_{Mn} - 356,861 x^{\gamma}_{C})}{RT}\right] \quad [9]$$

$$D^{\alpha}_{Si} = 1.06044 \cdot \exp\left[\frac{-(225,655 - 194,642 x^{\alpha}_{Si})}{RT}\right] \quad [10]$$

$$D^{\gamma}_{Si} = 0.05101 \cdot \exp\left[\frac{-238,838}{RT}\right] \quad [11]$$

The optimized functions of Eqs. [4] through [11] have been validated with the measurements in Figures 8 through 11, showing good agreement. Note that for the sake of clarity, only part of the original measurements of Table III have been shown in these figures.

C. Microstructure Data

The local solidification event is controlled by the secondary dendrite arms rather than the primary ones.[63] Conventionally, secondary dendrite arm spacing, SDAS, depends on the cooling rate, CRT, according to empirical equation SDAS = $a \cdot CRT^{-n}$, where a and n are material constants.[63] The experimental values of exponent n vary between 0.3 and 0.5, whereas the

theoretical value is 1/3. In the IDS tool, the effect of composition has been taken into account by adding a composition term to the given equation. Applying the available experimental data for numerous low and high alloyed steels,[64–78] the following function was optimized:

$$SDAS = 270 \cdot CRT^{-0.3} \cdot \exp(-A^{0.35}), \quad [12]$$

where SDAS is in μm, and CRT is the cooling rate in °C/s. For steels containing Al, Mn, Si, and C, the composition term of A takes the form of

$$A = 1.5727 \, C_C - 0.35914 \, C_C^2 + 0.0222 \, C_{Si} + 0.1230 \, C_{Mn} + 0.01 \, C_{Al} C_{Mn}, \quad [13]$$

where C_i is the solute composition in wt pct. The optimized function of Eq. [12] has been validated with the measurements of some Fe-Al-Mn-Si-C alloys in Figure 12 showing a reasonable agreement.
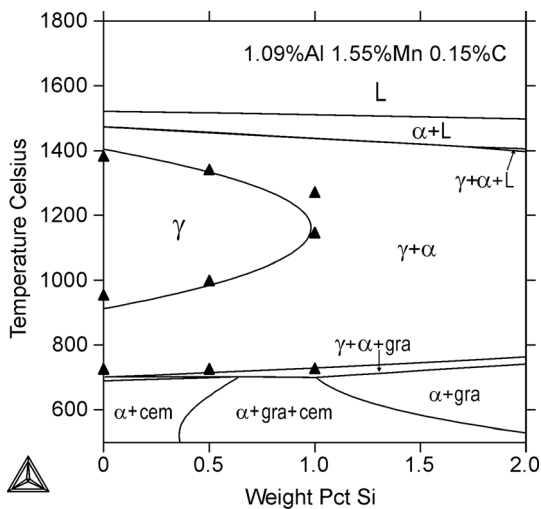

Fig. 8—Calculated Al diffusivity in ferritic (α) and austenitic (γ) iron, with experimental datapoints of Gröbner,[43] Vignes,[44] Bergner and Khaddour,[46] and Fridberg et al.[56] The type of experimental diffusion coefficient is defined as i impurity diffusion, c chemical diffusion, and e estimated diffusion.

Fig. 7—Calculated[18] vertical section of 1.09 wt pct Al-1.55 wt pct Mn-0.15 wt pct C in the Fe-Al-Mn-Si-C system, with the experimental datapoints of Gajda and Lis.[40]
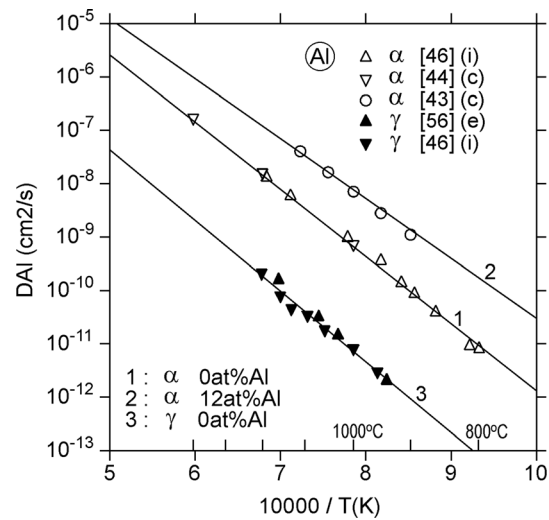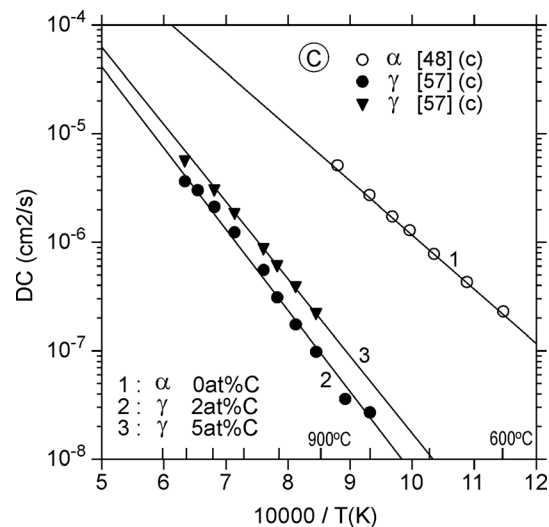

Fig. 9—Calculated C diffusivity in ferritic (α) and austenitic (γ) alloys, with the experimental datapoints of Smith[48] and Wells et al.[57] The type of experimental diffusion coefficient is defined as c chemical diffusion.

Table III. Composition Ranges of the Selected Experimental Measurements[43–62] on Solute Diffusion in Ferritic and Austenitic Iron

Phase	Ferrite		Austenite	
Solute	Range	References	Range	References
Al	0 to 12 at. pct Al	43 through 46	0 to 0.1 at. pct Al	46 and 56*
C	0 to 0.1 at. pct C	47 through 49	0 to 7 at. pct C	57
Mn	0 to 2 at. pct Mn	50 and 51	0 to 30 at. pct Mn	50, 58, and 59
Si	0 to 9 at. pct Si	52 through 55	0 to 1 at. pct Si	56*, 60 through 62

* denotes an estimate.

III. EXPERIMENTAL MEASUREMENTS AND THEIR COMPARISON WITH IDS CALCULATIONS

Experimental measurements were taken to determine the Mn composition (microsegregation) and ferrite content in two experimental casts of high-AlMnSi steels, using a field emission electron probe microanalyzer (FE-EPMA) (JEOL JXA-8530FPlus, Tokyo, Japan), a laser scanning confocal microscope (LSCM) (VK-X200, Keyence Ltd, Itasca), and the thermo-mechanical physical simulation system, Gleeble (Gleeble 3800, Dynamic Systems Inc., New York). The nominal compositions of
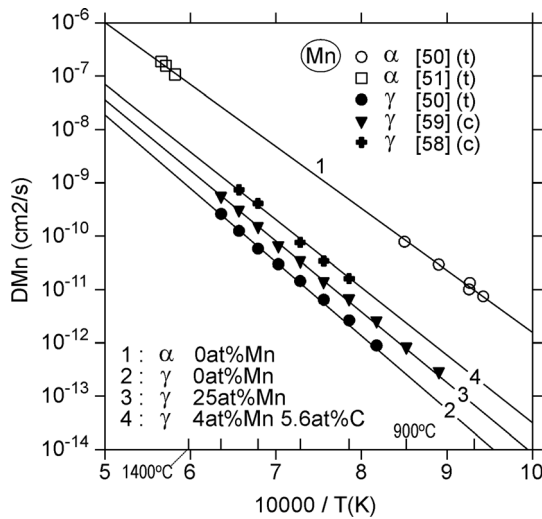

Fig. 10—Calculated Mn diffusivity in ferritic (α) and austenitic (γ) alloys, with the experimental datapoints of Nohara and Hirano,[50,59] Kirkaldy et al.,[51] and Wells and Mehl.[58] The type of experimental diffusion coefficient is defined as *t* tracer diffusion and *c* chemical diffusion.
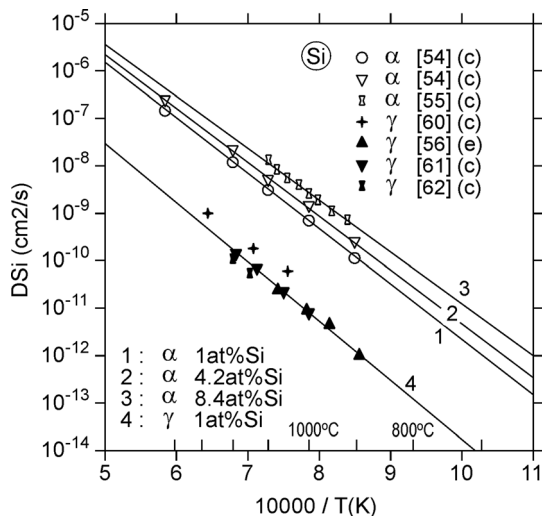

Fig. 11—Calculated Si diffusivity in ferritic (α) and austenitic (γ) alloys, with the experimental datapoints of Borg and Lai,[54] Mirani and Maaskant,[55] Fridberg et al.,[56] Krishtal and Mokrova,[60] Bergner et al.,[61] and Zheng et al.[62] The type of experimental diffusion coefficient is defined as *c* chemical diffusion and *e* estimated diffusion.

the steels are presented in Table IV. Two 15 × 20 mm samples were cut from ¼ thickness of each casting. They were utilized for manganese composition measurement and secondary dendrite arm spacing (SDAS) determination with the EPMA. A line analysis method was used, with a line length of 5 mm and a step size of 1 μm. Additionally, two sets of ∅6 × 36 mm samples intended for Gleeble simulations were machined from the ¼-thickness location of the castings. These Gleeble-simulated samples were used to distinguish the delta ferrite content in different thermal paths. To this end, LSCM images from ×10, ×20 and ×50 magnifications were first used to obtain an overview of bulk microstructures, after which SEM images (inlens, 5 kV, 5 mm focus) were taken to properly identify the delta ferrite content. Microstructural images were taken, utilizing the LSCM after Villella etching. The delta ferrite and martensite structures were quantified from longitudinal sections of the samples. The measurements were compared with the calculations of IDS to validate the IDS tool for more illustrative calculations, as presented in Section V. Note that the IDS calculations in this section apply to the whole IDS database capacity, whereas those of Section V apply to the data introduced in Section III.

zFirst, from the as-cast structures of the studied samples, the average secondary dendrite arm spacing (SDAS) and the minimum and maximum manganese compositions were determined with the EPMA. The measured values are displayed in Table V with the values calculated with the IDS. A reasonable agreement was obtained between the calculated and measured SDAS and the Mn composition values by applying a cooling rate of 0.5 °C/s in the IDS calculations. This rate was later required to construct the complete cooling/heating procedure for the IDS calculations when comparing them with the measured ferrite content of the steels. It should be noted that the measured SDAS values are not
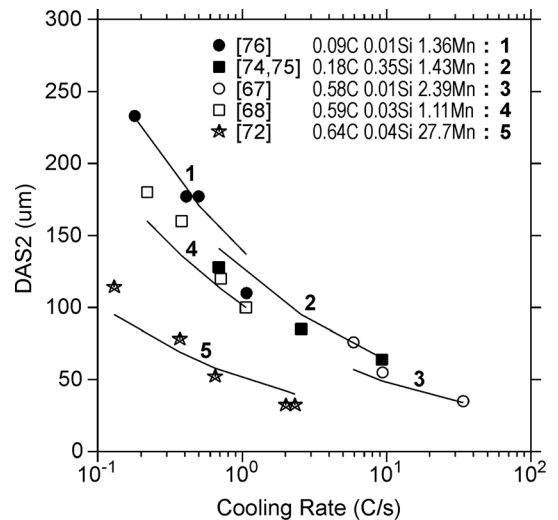

Fig. 12—Calculated secondary dendrite arm spacing in Mn-containing steels, with experimental datapoints of Schwerdtfeger,[67] Jacobi and Schwerdtfeger,[68] Taha et al.,[72] Imagumbai,[74, 75] and Jacobi and Wünnenberg.[76]

Table IV. Nominal Composition of the Investigated Steels, as Reported by the Steel Supplier (Measured by OES)

	Composition (Weight Percent)								
Steel	C	Si	Mn	Al	Cr	Ti	N	S	B
A	0.297	2.04	2.04	1.07	0.12	0.015	0.0051	0.0022	0.0005
B	0.292	1.97	3.78	0.91	0.03	0.014	0.0063	0.0036	0.0005

Table V. Measured (EPMA) and Calculated (IDS) Secondary Dendrite Arm Spacing (SDAS) and Mn Compositions of Dendrite Axis Ferrite (AX-α) and Interdendritic Austenite (ID-γ) in Steels A and B

	CRT (°C/s) Calc.	SDAS (μm)		Mn(AX-α) (Weight Percent)		Mn (ID-γ) (Weight Percent)	
Steel		Exp.	Calc.	Exp.	Calc.	Exp.	Calc.
A	0.5	132	128	1.55	1.58	2.35	2.44
B	0.5	115	120	2.75	2.62	4.25	4.68

The cooling rate for the calculations was 0.5 °C/s, and the Mn compositions refer to those calculated at 850 °C.
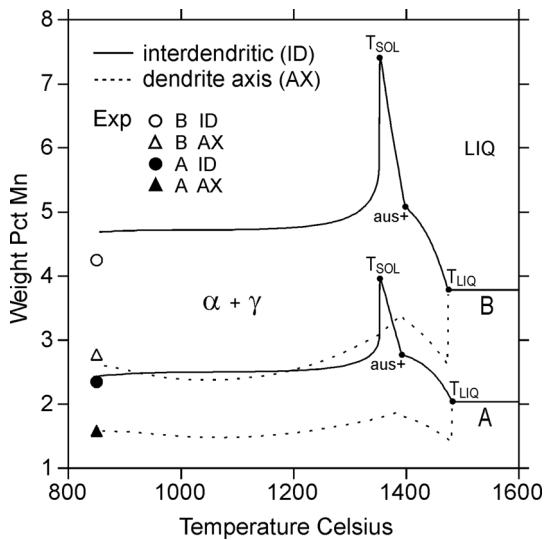

Fig. 13—Calculated (IDS) interdendritic (ID) and dendrite axis (AX) compositions of Mn in steels A and B, cooled at a rate of 0.5 °C/s, with Mn compositions measured (EPMA) in this study from the as-cast structure. T_{LIQ} liquidus temperature, T_{SOL} solidus temperature, aus + formation of austenite.

accurate, because they were estimated by the observed distances between the minimum and maximum Mn levels, assuming that these compositions corresponded to the center (axis) and surface of the secondary dendrite arm. Besides, the calculated Mn compositions refer to the values calculated at 850 °C (before the start of austenite decomposition), not the experimentally measured values at room temperature. However, as the Mn solid diffusion becomes sluggish below 850 °C (as indicated by Eq. 9), it is reasonable to assume that the Mn levels remain unaltered below that temperature.

A more illustrative presentation of the development of Mn compositions is presented in Figure 13, which shows how the calculated Mn compositions in the interdendritic region (solid line) and dendrite axis (dotted line) change with a decreasing temperature from the liquid state to 850 °C. During solidification, the enrichment of Mn in liquid is quite strong, especially after the formation of austenite, but below the solidus temperature, the high peaks of the interdendritic compositions collapse as soon as the last liquid drop disappears from the structure. Due to the limited Mn diffusion in austenite, however, the Mn level of the interdendritic region never reaches the nominal composition of the steel. Concerning the composition of the dendrite, there is a marked decrease in Mn content after the formation of austenite. This is due to the impoverishment of Mn in ferrite, which ultimately transforms to austenite. Finally, at 850 °C, the calculated Mn compositions agree quite well with the measured Mn compositions considering the complex stepwise calculations made with the IDS before reaching that temperature. Not even the calculated dendrite axis composition of steel B is a problem here, because the slight increase in Mn content ceases below 850 °C because of the limited kinetics.

The next step was to measure the ferrite content of the steel samples (A and B), quenched at temperatures of 1200 °C, 1000 °C, and 800 °C. The samples were first heated at 10 °C/s from room temperature to 1300 °C in a Gleeble simulator, held at that temperature for 90 seconds, and finally cooled to the quenching temperatures with three linear rates, 0.1 °C/s, 1 °C/s, and 10 °C/s. For example, Figure 14 shows the microstructures of steel A samples cooled at 0.1 °C/s and 10 °C/s to 800 °C. To compare the predicted measurements with the IDS calculations, the above-mentioned heating/cooling procedure was completed using the previously determined cooling rate of the solidification process (0.5 °C/s). The measured and calculated ferrite content is presented in Table VI. The agreement is very good (R^2 = 0.9 for steel A, and R^2 = 0.7 for steel B) considering the extensive calculations made by IDS during this cooling-heating-cooling treatment before reaching the quenching temperatures. The predictions for steel B
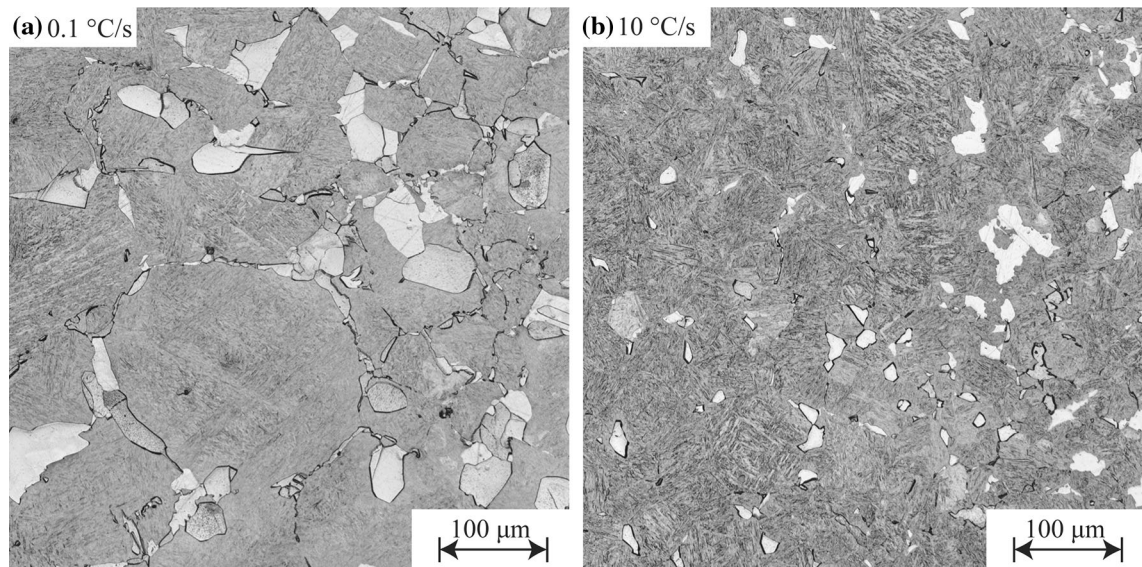
(a) 0.1 °C/s **(b)** 10 °C/s

100 μm   100 μm

Fig. 14—Microstructures of Gleeble-simulated samples quenched at 800 °C with cooling time of (*a*) 0.1 °C/s, (*b*) 10 °C/s. Vilella etching. LSCM-image. Ferritic structures are lighter; martensite structures are darker.

are approximately evenly under- or over-predicted, but for steel A, the ferrite pct appears to be somewhat over-predicted

A better illustration of this treatment is presented in Figure 15, which shows the results of IDS calculations from the liquid state to 800 °C and the measured ferrite content of Table VI. The solidification of both steels starts with the formation of ferrite, and a peritectic reaction occurs slightly below 1400 °C through the formation of austenite from the liquid and ferrite phases. The solidus temperature is reached in both steels at 1353 °C, which is purely coincidental, despite the different compositions of the two steels. During these calculations, the secondary dendrite arm spacing (SDAS) values were also estimated. They agree well with the measured values, as presented in Table VI. Below the solidus temperature, more ferrite is transformed to austenite, but below ~ 1150 °C, austenite starts to transform back to ferrite. The change of direction in the phase interface movement can be explained by the fact that at about 1150 °C, the austenitic iron reaches its maximal stability with regard to the ferritic iron. During the heating period (b), the positions of the α/γ phase interfaces are not the same as they were during the first cooling period (a). This is because a phase transformation controlled by kinetics is always irreversible, *i.e.*, any cooling or heating period leaves its impact on the results. Note also that the change from cooling (a) to heating (b) was made at 850 °C, because a further decrease in its value would have had only a minor effect on the development of the ferrite content. However, allowing this temperature to drop further to room temperature would have made the simulations too complex because of the onset of the austenite decomposition process below about 800 °C. Following heating at the holding temperature of 1300 °C, some ferrite is again transformed to austenite and below this temperature, during the final cooling periods (c and d), a procedure similar to

that of the first cooling period (a) occurs. The measured ferrite contents in Figure 15 are shown to agree well with the calculated curves of the final cooling periods. It should be noted that in both the steel structures, the final ferrite content decreased from the levels recorded in the first cooling period, but with a decreasing temperature, the ferrite content again increased—more effectively the lower the cooling rate. This behavior is logical when the calculations with those of the equilibrium solidification, illustrated by the broken lines of the α/γ phase interfaces in Figure 15, are compared. According to these lines (which, for sake of clarity, are only partially shown), both steels are fully austenitic within a certain temperature interval (around 1150 °C), but beyond these intervals, the ferrite content increases considerably when the temperature increases or decreases. This confirms the effect of kinetics in restraining the transformation speed, because the temperature variation during the non-equilibrium IDS calculations gives so little variation to the α/γ phase interface movement. However, prolonged heat treatment shifts the ferrite content close to its equilibrium value.

IV. SIMULATION RESULTS

The results of the IDS simulations are presented here for two high-AlMnSi steels containing C up to 1 wt pct, Mn 2 and 4 wt pct, Si 2 wt pct, and Al 1 wt pct. Of course, high-AlMnSi steels also contain small amounts of other elements, such as B, N, P, and S, which can be included in IDS simulations. However, this section focuses on describing the role of the basic solutes by applying the modeling data from Section III in the calculations.

Table VI. Experimental (Gleeble) and Calculated (IDS) Ferrite Fractions in Steels A and B, Cooled at Different Rates from 1300 °C, and Quenched at 1200 °C, 1000 °C, and 800 °C (1473 K, 1273 K, and 1073 K)

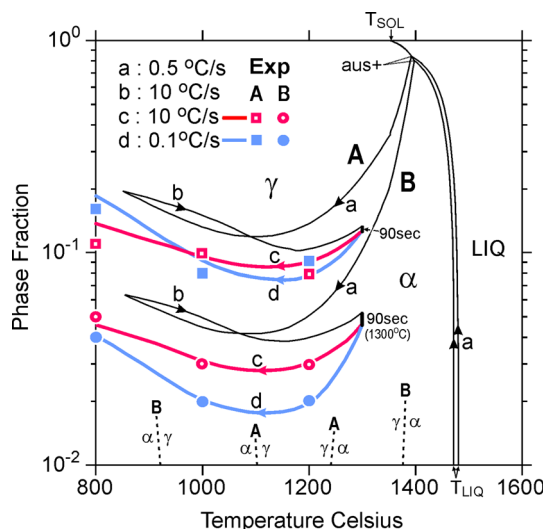| Steel	CRT (°C/s)	Pct Ferrite at 1200 °C		Pct Ferrite at 1000 °C		Pct Ferrite at 800 °C	
		Exp.	Calc.	Exp.	Calc.	Exp.	Calc.
A	0.1	8.8	7.8	9.0	9.2	16.4	17.6
	1	8.2	9.0	10.0	10.2	14.3	16.9
	10	8.3	9.1	9.8	9.6	11.3	13.4
B	0.1	2.0	1.9	2.0	2.0	3.9	3.6
	1	2.2	2.9	3.8	3.1	4.2	4.8
	10	2.8	3.0	3.0	3.1	4.7	4.3

Fig. 15—Calculated (IDS) phase fractions in steels A and B, with the ferrite fractions (datapoints) measured from the samples cooled with rates 10 °C/s and 0.1 °C/s to their quenching temperatures (1200 °C, 1000 °C, and 800 °C). Broken lines refer to the α/γ phase boundaries obtained by using the equilibrium solidification mode in calculations. T_{LIQ} liquidus temperature, T_{SOL} solidus temperature, aus + formation of austenite.
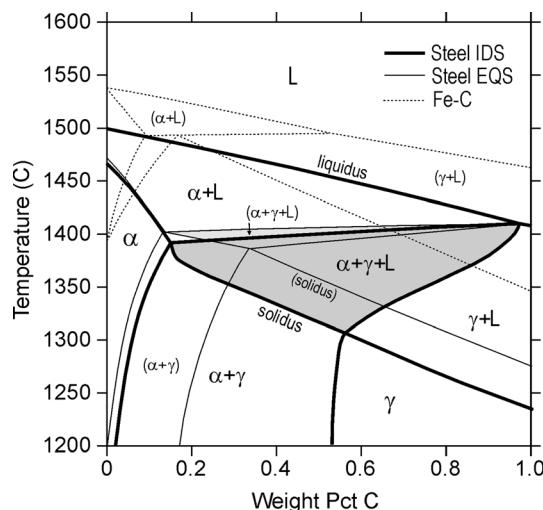

Fig. 16—Calculated dynamic phase diagram of steel C + 4 wt pct Mn + 2 wt pct Si + 1 wt pct Al, cooled at a rate of 1 °C/s (thick line). Also shown is the calculated dynamic phase diagram, according to equilibrium solidification (EQS) (thin line) and the Fe-C phase diagram (thin dotted line).

The effect of solutes on the high-temperature phase equilibria can be illustrated by a dynamic phase diagram for cooling. Using the IDS, a dynamic phase diagram can be constructed by conducting a series of IDS simulations with a changing nominal composition of the selected solute. The information obtained from a dynamic phase diagram is comparable to a vertical section calculated by some commercial thermodynamic software, apart from the fact that the latter pays no attention to the (finite) kinetics. Consequently, a vertical section can be produced by a single calculation, whereas the IDS simulations, which account for the kinetics, are always individual and independent of each other.

For an example of a dynamic phase diagram, see Figure 16, which illustrates the effect of carbon composition on the phase equilibria of high-AlMnSi steel containing 4 wt pct Mn, 2 wt pct Si, and 1 wt pct Al. The figure also shows (with dotted lines) the diagram calculated with an equilibrium mode comparable to a vertical section produced by thermodynamic software.

The differences between these two calculations are small for ferritic (α) solidification, which can be explained by the fast kinetics (i.e., high solute diffusivities) in ferrite. Instead, during austenitic solidification (γ), the differences become clear, as the solute diffusivities in austenite are much lower than in ferrite (see Figures 8 through 11). Note, especially, the much lower solidus, and the much wider $\alpha + \gamma + L$ and $\alpha + \gamma$ regions, when accounting for kinetics as well as the curvature of the $\alpha + \gamma + L$ region boundaries, untypical for a vertical section calculated with thermodynamic software. The wide $\alpha + \gamma$ region reveals the tendency of low solute diffusivities in austenite to restrain the movement of the α/γ phase transformation. Note also the much lower temperature region of both these diagrams with regard to the conventional Fe-C phase diagram.

The IDS tool can also be used to study the solute microsegregation, depending on the true cooling and heating processes. The solute microsegregation is best illustrated by the solute concentration profile calculated in the volume element of the model (Figure 1).
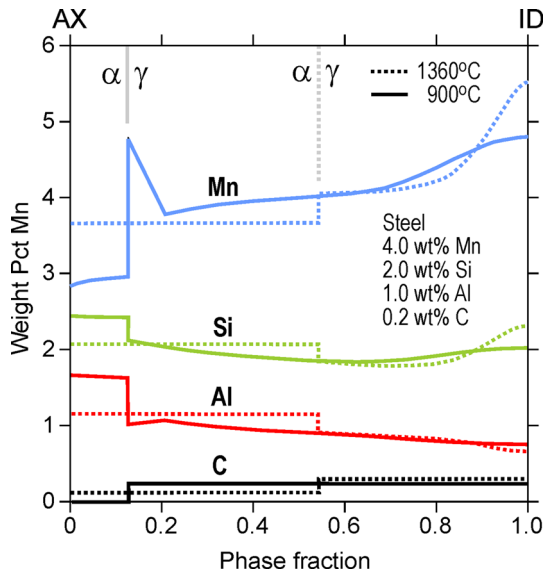
Fig. 17—Calculated concentration profiles of Mn, Si, Al, and C in steel containing 4 wt pct Mn + 2 wt pct Si + 1 wt pct Al + 0.2 wt pct C, cooled at a linear rate of 1 °C/s, at 1360 °C (1633 K) and 900 °C (1173 K). AX denotes the dendrite axis; ID denotes the interdendritic region of the volume element.

Figure 17 shows the calculated solute concentration profiles in high-AlMnSi steel containing 4 wt pct Mn, 2 wt pct Si, 1 wt pct Al, and 0.2 wt pct C. The profiles are presented at 1360 °C (some degrees below the solidus) and 900 °C (1173 K). The cooling rate employed in the calculation was 1 °C/s. The strong tendency of Mn to segregate in the interdendritic (ID) region is noteworthy. This is mainly due to its strong tendency to enrich in the liquid phase above the solidus. During cooling, the interdendritic Mn composition level is lowered by diffusion (see the solid line of Mn), but at the employed cooling rate, this lowering of Mn content is not very effective because of the low diffusivity of Mn in austenite. As Mn is a typical austenite stabilizer (though not very strong), its content in ferrite at the dendrite axis (AX) is lower than in austenite. As the ferrite fraction decreases with the temperature, the Mn content decreases even further, which is also a measure of microsegregation. However, the most interesting point in the Mn concentration profile is the strong Mn peak on the austenite side of the α/γ interface at 900 °C. This peak best reveals the poor diffusivity of Mn in austenite, as the Mn composition at the center of austenite no longer corresponds to the Mn composition of the moving interface. Yet it can be questioned how well the assumption of complete equilibrium holds at a phase interface at such a low temperature as 900 °C (1173 K). IDS assumes this for any phase interface (excluding those of the austenite decomposition process), and it can be expected to hold well only at high temperatures. In any case, the present calculations show that such a strong α/γ interface peak is formed for Mn, although it is much less wide (and the slope is much steeper) than shown in Figure 17. This is simply because of the low number of grid points used to present the concentration profiles.

For Si, the tendency of microsegregation, especially in the interdendritic region, is much lower than for Mn (Figure 17). This partly originates in the repulsive interaction between C and Si atoms in liquid, which prevents the enrichment of Si to an extent comparable to Mn. However, after the formation of austenite (above the solidus), the enrichment of Si in liquid is again accelerated due to the low diffusivity of Si in austenite. This leads to a higher Si composition in the interdendritic region, even below the solidus, whereas the Si level in the composition is still relatively low at some distance from the interdendritic region (see the dotted curve of Si in Figure 17). During cooling, the corresponding peak is homogenized quite effectively, close to the nominal Si composition of 2 wt pct Si. However, Si remains segregated in the scale of the whole volume element, with a slight minimum in the middle of austenite (at a phase fraction value of about 0.6) and a higher Si content in the axial ferrite (as Si tends to stabilize ferrite compared to austenite). Generally, however, the final concentration profile of Si at 900 °C (1173 K) is plateau-like and not far from the nominal Si composition of 2 wt pct.

For Al, the tendency of microsegregation in the interdendritic region is also low (Figure 17). But contrary to Si, its repulsion with C is so strong that Al will be strongly impoverished from the liquid phase. This impoverishment also continues after the formation of austenite. Thus, below the solidus, the interdendritic Al composition is very low (see the dotted curve of Al in Figure 17). Consequently, Al can be classified as a negatively segregating solute in high-AlMnSi steels. During cooling, the low interdendritic Al composition increases only slightly, because austenite has systematically been impoverished from Al close to the interdendritic region. At the dendrite axis, however, ferrite is strongly enriched by Al due to its strong tendency to stabilize ferrite. Al segregation therefore becomes stronger than that of Si. Note again the α/γ interface peak at 900 °C (1173 K), as in the case of Mn. The peak is now negative and much weaker than for Mn, but again because of the poor kinetics in austenite.

Finally, Figure 17 also shows the concentration profiles for carbon. In this case, note the uniform C content in both phases, austenite and ferrite, which is due to their high C diffusivity. Indeed, in most circumstances, IDS treats C as a lever-rule component, which is to say that its diffusion is assumed to be extremely rapid. At lower temperatures and under rapid cooling processes, however, C behaves more like a normal solute, having finite diffusivity. This is a reasonable strategy made to simplify the mathematical treatments of diffusion in IDS. Thus, at relatively low cooling rates and temperatures above 900 °C (1,173 K), the segregation tendency of C is only due to the presence of the α/γ interface. After the disappearance of this interface, there will be no microsegregation of C in the structure.

Further calculations were made to study the effect of the cooling rate on interdendritic solute compositions. The results of the calculations made for a high-AlMnSi steel containing 4 wt pct Mn, 2 wt pct Si, 1 wt pct Al, and 0.3 wt pct C, using three constant cooling rates (0.1

Table VII. Calculated Interdendritic Solute Compositions, C_i^{ID}, in Wt Pct at Different Temperatures and Cooling Rates in Steel 4 Wt Pct Mn + 2 Wt Pct Si + 1 Wt Pct Al + 0.3 WT Pct C

Solute	Temp. (°C)	Cooling Rate			
		0.1 °C/s	1 °C/s	10 °C/s	Modified*
Mn	1330	5.08	5.73	6.68	
(4 Wt Pct)	1200	4.77	5.25	5.92	4.75
	900	4.73	5.19	5.84	4.52
Si	1350	2.23	2.50	2.91	
(2 Wt Pct)	1200	2.09	2.27	2.56	2.05
	900	2.08	2.25	2.53	1.99
Al	1330	0.72	0.63	0.51	
(1 Wt Pct)	1200	0.76	0.71	0.63	0.81
	900	0.78	0.72	0.64	0.85
C	1330	0.338	0.341	0.344	
(0.3 Wt Pct)	1200	0.314	0.317	0.318	0.313
	900	0.318	0.320	0.320	0.315
Solidus Temperature (°C)		1,358	1,350	1,340	1,340
Ferrite Content at 900 °C (Pct)		6.15	6.75	7.00	5.14

Also shown, at the same cooling rates, are the calculated solidus temperatures and ferrite contents at 900 °C (1173 K).
*Modified cooling: 10 °C/s at 1600 °C to 1200 °C (1873 K to 1473 K), 10-min holding at 1200 °C (1473 K), 0.1 °C/s below 1200 °C (1473 K).

Table VIII. Calculated Properties in Steel 2 Wt Pct Si + 1 Wt Pct Al with 2 and 4 Wt Pct Mn and 0.1 to 0.3 Wt Pct C

2 Wt Pct Mn	0.1 Wt Pct C	0.2 Wt Pct C	0.3 Wt Pct C
T_{LIQ} (°C)	1500	1492	1483
T_{ZST} (°C)	1470	1446	1419
T_{AUS} (°C)	1335	1394	1396
T_{SOL} (°C)	1432	1374	1358
SDAS(μm)	125	115	108
Ferrite (α) Content at Solidus (Pct)	100	73	35
Ferrite (α) Content at 900 °C (Pct)	53	28	15
C_{Mn} (wt pct)*	1.71/2.19	1.59/2.33	1.51/2.56
C_{Si} (Wt Pct)*	2.20/1.76	2.37/1.92	2.52/2.16
C_{Al} (Wt Pct)*	1.24/0.78	1.39/0.80	1.52/0.76
4 Wt Pct Mn	0.1 wt pct C	0.2 wt pct C	0.3 wt pct C
T_{LIQ} (°C)	1490	1482	1474
T_{ZST} (°C)	1457	1433	1408
T_{AUS} (°C)	1353	1392	1395
T_{SOL} (°C)	1419	1367	1350
SDAS (μm)	109	103	98
Ferrite (α) content at solidus (pct)	100	60	24
Ferrite (α) content at 900 °C (1173 K) (pct)	24	13	7
C_{Mn} (Wt Pct)*	3.03/4.41	2.83/4.80	2.67/5.19
C_{Si} (Wt Pct)*	2.28/1.83	2.44/2.03	2.59/2.25
C_{Al} (Wt Pct)*	1.51/0.78	1.67/0.76	1.82/0.72

The cooling rate of calculations was 1 °C/s.
LIQ liquidus, *ZST* zero strength, *AUS* austenite, *SOL* solidus, *SDAS* secondary dendrite arm spacing.
*Axial (α) composition/interdendritic (γ) composition at 900 °C (1173 K).

°C/s, 1 °C/s, and 10 °C/s) and modified cooling, are presented in Table VII (see the table footnote for the modified cooling). Increasing the cooling rate systematically increases the interdendritic Mn and Si compositions, and decreases the interdendritic Al composition. It thus increases the degree of microsegregation. This is, of course, due to the reduced time for solute diffusion in austenite. Even the finer secondary dendrite arm spacing, caused by the higher cooling rate, is incapable of compensating for this trend, although some compensation does occur due to the reduced diffusion distances in the dendrite arm. The much stronger homogenization of

solute compositions at a temperature interval of 1330 °C to 1200 °C (1603 K to 1473 K) than at an interval of 1200 °C to 900 °C (1473 K to 1173 K) is also noteworthy. This indicates how poor the solute diffusion rate becomes in austenite at low temperatures. Through modified cooling (CRT = 10 °C/s at 1600 °C to 1200 °C [1873 K to 1473 K], maintained for 10 minutes at 1200 °C [1473 K] and CRT = 0.1 °C/s below 1200 °C [1473 K]), the interdendritic solute compositions were reduced considerably, but such a treatment is difficult to arrange during conventional solidification processes, such as continuous casting. The situation differs if the as-cast

product is heat-treated afterwards in a controlled way, but even in this case, there is a risk that the austenite grains grow too large during the treatment. It is noteworthy that for C, the interdendritic composition in austenite is higher than the nominal one, essentially because of the presence of ferrite. Otherwise, these compositions are almost identical, also indicating good diffusion kinetics for C at a high cooling rate of 10 °C/s. Table VII also presents the effect of the cooling rate on the solidus temperature and content of ferrite at 900 °C (1173 K). Increasing the cooling rate from 0.1 °C/s to 1 °C/s and from 1 °C/s to 10 °C/s causes the solidus temperature to drop by only 8 °C and 10 °C, respectively. Larger drops in the solidus temperature can be obtained by applying an exponent value lower than 0.3 for the cooling rate CRT of Eq. [12]. However, as this is already a minimum value suggested in the literature,[57] no steps were taken to increase the effect of the cooling rate on solidification. The ferrite content at 900 °C is also weakly dependent on the cooling rate. Its value in Table VII is around 6 pct after all four cooling processes. Through an appropriate post-heat treatment, however, the ferrite content can still be influenced, as Figure 15 demonstrates.

As Table VII shows, the effect of the cooling rate on the results of the high-AlMnSi steels is clearly visible only for solute microsegregation. To study the effect of composition, three different carbon compositions of 0.1, 0.2, and 0.3 wt pct C were used for two different high-AlMnSi steels containing 2 and 4 wt pct Mn, 2 wt pct Si, and 1 wt pct Al. Some essential results of the IDS simulations are presented in Table VIII. As expected, increasing the carbon composition significantly changes the temperatures of liquidus, zero strength (75 pct of the local structure is solidified[79]), austenite formation, and solidus. For the 2 wt pct Mn steel, these temperatures are higher than those for the 4 wt pct Mn steel. The only exception is the lower temperature value of austenite formation in alloy 2 wt pct Mn + 0.1 wt pct C, which is due to the lower capacity of 2 wt pct Mn alloying to stabilize the austenite. Increasing the carbon composition also affects the value of the secondary dendrite arm spacing, SDAS, by decreasing its value according to the optimized Eq. [2]. It also quite effectively decreases the fraction of ferrite, both at the solidus temperature and at 900 °C (1173 K). Obviously, this is due to the strong tendency of C to stabilize the austenite. Indeed, carbon alloying seems the most effective way to achieve an ideal phase structure for high-AlMnSi steels before their further treatment at low temperatures, *e.g.*, during the austenite decomposition process. Carbon composition also greatly influences the interdendritic and axial solute compositions. For Mn, Si, and Al, Table VIII shows two values for each carbon composition value, the first corresponding to the dendrite axis ferrite composition, and the second to the interdendritic austenite composition. By increasing the C content, the dendrite axis ferrite composition in the Mn level decreases, whereas the corresponding Si and Al content increases as a consequence of the decreasing ferrite content of the structure. This trend is expected, because solute atoms always tend to concentrate in the phase in which they

stabilize, even the disappearing one. Instead, the interdendritic austenite compositions all increase as the C content increases. However, for Al, this is no longer true between 0.2 and 0.3 wt pct C. Generally, it can be concluded that increasing carbon composition increases the microsegregation tendency of each solute in the high-AlMnSi steels of Table VIII. This may place some restrictions on the change in the carbon composition when seeking an optimal phase structure for the high-AlMnSi steel before its post treatments at lower temperatures.

Finally, as the Mn, Si, and Al alloying in high-AlMnSi steels is higher than in typical carbon steels, it is interesting to compare their sensitivity to cracking. Recently, several quality indices were developed to describe this sensitivity in solidifying steels.[80] For example, we made calculations for two of these indices, QI_{STR} and QI_{SHE}, which are associated with the disturbed strengthening above the solidus (QI_{STR}) and the disturbed shell growth below it (QI_{SHE}). Both events originate in the contraction related to the phase transformation from ferrite to austenite. If the amount of the forming austenite is high, steel is highly sensitive to defects like longitudinal surface cracking (facial and corner), transverse corner cracking, hot cracking, and bleeding. The indices QI_{STR} and QI_{SHE} are described as[80]

$$QI_{STR} = 65(f_{max}^{\alpha,Z} - f_{SOL}^{\alpha}) \qquad [14]$$

$$QI_{SHE} = 43(f_{SOL}^{\alpha} - f_{max}^{\alpha,S}), \qquad [15]$$

where coefficients $^6/_5$ and $^4/_3$ are calibration factors, f_{SOL}^{α} is the ferrite fraction at the solidus, $f_{max}^{\alpha,Z}$ is the maximal ferrite fraction between the zero-strength temperature and the solidus, and $f_{max}^{\alpha,S}$ is the maximal ferrite fraction between the solidus and the solidus
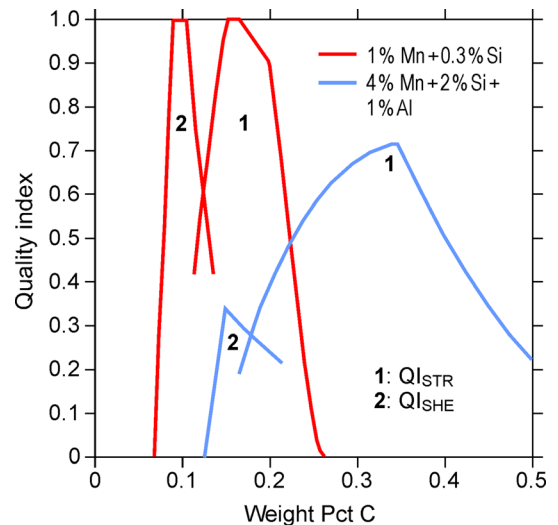

Fig. 18—Effect of carbon composition on the quality indices QI_{STR} and QI_{SHE} in carbon steel of 1 wt pct Mn + 0.3 wt pct Si and high-AlMnSi steel of 4 wt pct Mn + 2 wt pct Si + 1 wt pct Al, cooled at 1 °C/s.

– 30 °C. All these phase fractions are calculated using IDS. The indices QI_{STR} and QI_{SHE} obtain values between 0 and 1 to ensure that increasing values indicate weakened quality in relation to the disturbed strengthening and shell growth, respectively.

Figure 18 shows the effect of carbon content on the QI_{STR} and QI_{SHE} indices in a carbon steel of 1 wt pct Mn + 0.3 wt pct Si and in a high-AlMnSi steel of 4 wt pct Mn + 2 wt pct Si + 1 wt pct Al. Note the maxima of QI_{STR} and QI_{SHE} at about 0.10 wt pct C and 0.16 wt pct C for the carbon steel, and the lower maxima at about 0.15 wt pct C and 0.34 wt pct C for the high-AlMnSi steel. Consequently, the cracking sensitivity in the latter steel is much lower than in the former—up to 0.20 wt pct C. Increasing the carbon content above 0.3 wt pct, however, also makes the high-AlMnSi steel sensitive to cracking *via* index QI_{STR}. The results for the high-AlMnSi steel containing 2 wt pct Mn differ little from those of the 4 wt pct Mn-containing steel.

V. CONCLUSIONS

In this study, thermodynamic, kinetic, and microstructure data were presented for the modeling of solidification Fe-Al-Mn-Si-C alloys. These data were exhaustively validated by experimental measurements. The data were then applied in thermodynamic–kinetic software, IDS, to test their validity for modeling the solidification of high-AlMnSi steels. The IDS simulations were found to align well with the EPMA measurements of the present study. These results revealed that the residual ferrite content in a high-AlMnSi steel can be modified with appropriate heat treatment, and that the content is very far from that calculated by thermodynamic software that pays no attention to kinetics. Finally, example simulations were made with the IDS software to study the effect of alloying and the cooling rate on the solidification behavior of high-AlMnSi steels. These results reveal the following trends:

1. The solidification event in high-AlMnSi steels occurs at much lower temperatures than in carbon steels. The solidus drops especially in those high-AlMnSi steels whose austenite fraction above the solidus is high. The main reason is the strong tendency of Mn to enrich in the liquid phase in austenite-containing alloys.
2. Increasing the cooling rate decreases the solidus, but not by much. This is due to the optimized algorithm of the secondary dendrite arm spacing, which improves the diffusion kinetics at high cooling rates by shortening the diffusion distances in a thinner dendrite arm.
3. After solidification, the interdendritic Mn content in austenite is relatively high and does not homogenize very effectively due to the slow diffusivity of Mn in austenite. The interdendritic Si and Al compositions in austenite are much lower due to their tendency to deplete from the liquid phase. For Al, the tendency is so strong that Al can be classified as a completely negatively segregating solute, *i.e.*, the interdendritic composition of Al is the lowest content in its solid-state concentration profile.
4. The strengthening above the solidus and the shell growth below the solidus (as described by the quality indices QI_{STR} and QI_{SHE}, respectively) are much less disturbed in high-AlMnSi steels containing less than 0.2 wt pct carbon than in plain carbon steels. The cracking tendency in high-AlMnSi steels is therefore lower than in carbon steels, but no longer at carbon compositions exceeding 0.2 wt pct.

As the decomposition of austenite is expected to start from the interdendritic regions (grain boundaries) and to depend on the soluble alloy compositions in these regions, the present simulation results at 900 °C (1173 K) form a realistic starting point for further simulations of austenite decomposition at lower temperatures.

OPEN ACCESS

NOMENCLATURE

SUBSCRIPTS AND ABBREVIATIONS

AUS	Austenite
AX	Dendrite arm axis
ID	Interdendritic region

L   Liquid phase
LIQ   Liquidus
PE R   Peritectic
SOL   Solidus
ZST   Zero strength (75 pct of the local structure is solidified)

SYMBOLS AND VARIABLES

C_i	Solute composition (wt pct)
C_i^{ID}	Interdendritic solute compositions (wt pct)
CRT	Cooling rate (°C/s)
D	Diffusion coefficient (m^2/s)
f^{α}_{SOL}	Ferrite fraction at the solidus
$f_{max}^{\alpha,Z}$	Maximal ferrite fraction between the zero-strength temperature and the solidus
$f_{max}^{\alpha,S}$	Maximal ferrite fraction between the solidus and the solidus $-$ 30 °C
$^{\circ}G$	Gibbs free energy (J/mol)
L	Interaction parameter (J/mol)
n	Number of components in the alloy
QI_{SHE}	Quality index for disturbed shell growth below the solidus
QI_{STR}	Quality index for disturbed strengthening above the solidus
R	Gas constant [J/(K mol)]
SDAS	Secondary dendrite arm spacing (μm)
t	Time (seconds)
T	Temperature (K)
x_i	Mole fraction of component i
α	Ferrite
β	Composition-dependent parameter related to the total magnetic entropy
μ_i^{ϕ}	Chemical potential of the component i in phase ϕ,
γ	Austenite

REFERENCES

1. N. Baluch, Z.M. Udin, and C.S. Abdullah: *Eng. Tech. Appl. Sci. Res.*, 2014, vol. 4, pp. 686–89.
2. S. Louhenkilpi: *Continuous Casting of Steel,* pp. 373–434, Anonymous Treatise on Process Metallurgy, Volume 3: Industrial Processes, Elsevier, Oxford, 2014.
3. J. Miettinen, S. Koskenniska, M. Somani, S. Louhenkilpi, A. Pohjonen, J. Larkiola, and J. Kömi: *Metall. Mater. Trans. B*, 2019, vol. 50, pp. 2853–66.
4. J. Miettinen: *Metall. Trans. A*, 1992, vol. 23, pp. 1155–70.
5. J. Miettinen: 1999, TKK-MK-78.
6. J. Miettinen, S. Louhenkilpi, H. Kytönen, and J. Laine: *Math. Comp. Simul.*, 2010, vol. 80, pp. 1536–50.
7. J. Miettinen, S. Louhenkilpi, V.-V. Visuri, and T. Fabritius: *IOP Conf. Ser. Mater. Sci. Eng.*, 2019, vol. 529, p. 012063.
8. S. Louhenkilpi, J. Miettinen, J. Laine, R. Vesanen, I. Rentola, J. Moilanen, V.-V. Visuri, E.-P. Heikkinen, and A. Jokilaakso: *IOP Conf. Ser. Mater. Sci. Eng.*, 2019, vol. 529, p. 012051.
9. Y. Ueshima, S. Mizoguchi, T. Matsumiya, and H. Kajioka: *Metall. Trans. B*, 1986, vol. 17, pp. 845–59.
10. H. Lukas, S.G. Fries, and B. Sudman: *Computational Thermodynamics: The Calphad Method*, Cambridge University Press, Cambridge, 2007.
11. M. Hillert and M. Jarl: *Calphad*, 1978, vol. 2, pp. 227–38.
12. T. Åkermark: *Diploma Work*, KTH Royal Institute of Technology, Stockholm, 1991.
13. J.-O. Andersson and J. Ågren: *J. Appl. Phys.*, 1992, vol. 72, pp. 1350–55.
14. J. Ågren: *ISIJ Int.*, 1992, vol. 32, pp. 291–96.
15. B. Jönsson: *Z. Metallkd.*, 1992, vol. 83, pp. 349–55.
16. B. Jönsson: *Z. Metallkd.*, 1994, vol. 85, pp. 498–509.
17. B. Jönsson: *Scand. J. Metall.*, 1995, vol. 24, pp. 21–27.
18. J. Miettinen, V.-V. Visuri, and T. Fabritius: *Acta Univ. Oul. C,* 2019, vol. 704.
19. O. Redlich and A.T. Kister: *Ind. Eng. Chem.*, 1948, vol. 40, pp. 345–48.
20. A.T. Dinsdale: *Calphad*, 1991, vol. 15, pp. 317–425.
21. K.C. HariKumar and V. Raghavan: *J. Phase Equilib.*, 1991, vol. 12, pp. 275–86.
22. X.J. Liu, I. Ohnuma, R. Kainuma, and K. Ishida: *J. Phase Equilib.*, 1999, vol. 20, pp. 45–56.
23. J. Gröbner, H.L. Lukas, and F. Aldinger: *Anonymous COST 507—Thermochemical Database for Light Metal Alloys*, European Communities, Belgium, 1998, vol. 2.
24. P. Gustafson: *Scand. J. Metall.*, 1985, vol. 14, pp. 259–67.
25. D. Djurovic, B. Hallstedt, J. von Appen, and R. Dronskowski: *Calphad*, 2010, vol. 3, pp. 129–33.
26. W. Huang: *Calphad*, 1989, vol. 13, pp. 243–52.
27. J. Miettinen: *Calphad*, 1998, vol. 22, pp. 231–56.
28. J.E. Tibbals: Anonymous COST 507—Thermochemical database for light metal alloys, Volume 2, European Communities, Belgium, 1998, pp. 236–40.
29. R. Umino, X.J. Liu, Y. Sutou, C.P. Wang, I. Ohnuma R. Kainuma, and K. Ishida: *J. Phase Equilib.*, 2006, vol. 27, pp. 54–62.
30. J. Lacaze and B. Sundman: *Metall. Trans. A*, 1991, vol. 22, pp. 2211–23.
31. L. Li, S. Huang, L. Wang, Y.-L. He, J. Vleugels, and O. van der Biest: *Front. Mater. Sci. China*, 2009, vol. 3, pp. 33–37.
32. P. Presoly, R. Pierer, and C. Bernhard: *Metall. Trans. A*, 2013, vol. 22, pp. 5377–88.
33. T. Wada, H. Wada, J.F. Elliott, and J. Chipman: *Metall. Trans.*, 1972, vol. 3, pp. 1657–62.
34. D. Djurovic, B. Hallstedt, J. von Appen, and R. Dronskowski: *Calphad*, 2011, vol. 35, pp. 479–91.
35. R.P. Smith: *J. Am. Chem. Soc.*, 1948, vol. 70, pp. 2724–29.
36. E. Schürmann, T. Schmidt, and F. Tillman: *Giessereiforschung*, 1967, vol. 19, pp. 25–34.
37. K. Ishida, H. Ohtani, N. Satoh, R. Kainuma, and T. Nishizawa: *ISIJ Int.*, 1990, vol. 30, pp. 680–86.
38. I. Fartushna, I. Bajenova, A. Khvan, V. Cheverikin, D. Ivanov, S. Shilundeni, A. Alpatov, K. Sachin, and B. Hallstedt: *J. Alloys Compd.*, 2018, vol. 735, pp. 1211–18.
39. P. Presoly, G. Xia, P. Reisinger, and C. Bernhard: *Berg- U. Hüttenmänn. Monatsh.*, 2014, vol. 159, pp. 430–37.
40. B. Gajda and A.K. Lis: *Arch. Mater. Manuf. Eng.*, 2007, vol. 20, pp. 439–42.
41. K.-G. Chin, H.-J. Lee, J.-H. Kwak, Y.-J. Kang, and B.-J. Lee: *J. Alloys Compd.*, 2010, vol. 505, pp. 217–23.
42. M.S. Kim and Y.B. Kang: *J. Phase Equilib. Diff.*, 2015, vol. 36, pp. 453–70.
43. P. Gröbner: *Hutnicke Listy*, 1955, vol. 10, pp. 200–02.
44. A. Vignes: *Trans. 2nd National Conference on Electron Microprobe Analysis*, Boston, MA, 1967, pp. Paper No. 20.
45. K. Hirano and A. Hishunima: *J. Jpn. Inst. Met.*, 1968, vol. 32, pp. 516–21.
46. D. Bergner and Y. Khaddour: *Def. Diff. Forum*, 1993, vols. 95–98, pp. 709–14.
47. J.K. Stanley: *Trans. Met. Soc. AIME*, 1949, vol. 185, pp. 752–61.
48. R.P. Smith: *Trans. Met. Soc. AIME*, 1962, vol. 224, pp. 105–11.
49. A.E. Lord: *J. Acoust. Soc. Am.*, 1969, vol. 45, p. 1382.
50. K. Nohara and K. Hirano: *Suppl. Trans. Iron Steel Inst. Jpn.*, 1971, vol. 11, pp. 1267–73.
51. J.S. Kirkaldy, P.N. Smith, and R.C. Sharma: *Metall. Trans.*, 1973, vol. 4, pp. 624–25.
52. W. Batz, H.W. Mead, and C.E. Birchenall: *J. Met.*, 1952, vol. 4, p. 1070.
53. H. Mitani, M. Onishi, and T. Shikano: *J. Jpn. Inst. Met.*, 1966, vol. 30, pp. 56–61.
54. R.J. Borg and D.Y.F. Lai: *J. Appl. Phys.*, 1970, vol. 41, pp. 5193–5200.

55. H.V.M. Mirani and P. Maaskant: *Phys. Stat. Solidi A*, 1972, vol. 14, pp. 521–25.
56. J. Fridberg, L.-E. Törndahl, and M. Hillert: *Jernkontores Ann.*, 1969, vol. 153, pp. 263–76.
57. C. Wells, W. Batz, and R.F. Mehl: *Trans. AIME J. Met.*, 1950, vol. 188, pp. 553–60.
58. C. Wells and R.F. Mehl: *Trans. Am. Inst. Min. Eng.*, 1941, vol. 145, pp. 315–28.
59. K. Nohara and K. Hirano: *J. Jpn Inst. Met.*, 1973, vol. 37, p. 51.
60. M. A. Krishtal and A. M. Mokrova: *Metalloved. i. Term. Obrabot. Metall.,* vol. 2, p. 5.
61. D. Bergner, Y. Khaddour, and S. Lörx: *Def. Diff. Forum*, 1989, vols. 66–69, pp. 1407–12.
62. W. Zheng, X.-G. Lu, Y. He, Y. Cui, and L. Li: *J. Alloys Compd.*, 2015, vol. 632, pp. 661–75.
63. W. Kurz and D.J. Fisher: *Fundamentals of Solidification*, Trans Tech Publications, Aedermannsdorf, 1989.
64. A. Suzuki, T. Suzuki, Y. Nakaoga, and Y. Iwata: *J. Jpn. Inst. Met.*, 1968, vol. 32, pp. 1301–05.
65. A. Suzuki and Y. Nakaoga: *J. Jpn. Inst. Met.*, 1969, vol. 33, pp. 658–63.
66. M.C. Flemings, D.R. Poirier, and R.V. Barone: *J. Iron Steel Inst.*, 1970, vol. 208, pp. 371–81.
67. K. Schwerdtfeger: *Arch. Eisenhüttenwes.*, 1970, vol. 41, pp. 923–37.
68. H. Jacobi and K. Schwerdtfeger: *Metall. Trans. A*, 1976, vol. 7, pp. 811–20.
69. Jernkontoret: *A guide to the solidification of steels,* Jernkontoret, Stockholm, Sweden, 1977.
70. T. Okamoto, S. Matsuo, and K. Kishitake: *Tetsu-to-Hagané*, 1977, vol. 63, pp. 936–42.
71. M. Wolf: Doctoral thesis, École polytechnique fédérale de Lausanne, Lausanne, 1978.
72. M.A. Taha, H. Jacobi, M. Imagumbai, and K. Schwerdtfeger: *Metall. Trans. A*, 1982, vol. 13, pp. 2131–41.
73. B. Rogberg: *Segregation and Structure in Continuously Cast 1% Carbon Steel*, AB Sandvik Steel, Stockholm, Sweden, 1984.
74. M. Imagumbai: *ISIJ Int.*, 1994, vol. 134, pp. 574–83.
75. M. Imagumbai: *ISIJ Int.*, 1994, vol. 134, pp. 896–905.
76. H. Jacobi and K. Wünnenberg: *Steel Res.*, 1999, vol. 70, pp. 362–67.
77. B. Weisberger, M. Hecht, and K. Harste: *Steel Res.*, 1999, vol. 70, pp. 403–11.
78. M. Kudoh and B. Wo: *Steel Res.*, 2003, vol. 74, pp. 161–67.
79. Y.M. Won, K.-H. Kim, T.-J. Yeo, and K.H. Oh: *ISIJ Int.*, 1998, vol. 38, pp. 1093–99.
80. S. Louhenkilpi, J. Miettinen, V.-V. Visuri, M.C. Somani, S. Koskenniska, and T. Fabritius: *Ironmak. Steelmak.*, 2020, https://doi.org/10.1080/03019233.2020.1758994.